scientific reports

Check for updates

OPEN

Interpretable prediction of drug synergy for breast cancer by random forest with features from Boolean modeling of signaling pathways

Kittisak Taoma[1,2], Marasri Ruengjitchatchawalya[1,3], Kanthida Kusonmano[1,4], Teerasit Termsaithong[5,6], Thana Sutthibutpong[6,7], Monrudee Liangruksa[8] & Teeraphan Laomettachit[1,6]✉

Breast cancer is a complex and challenging disease to treat, and despite progress in combating it, drug resistance remains a significant hindrance. Drug combinations have shown promising results in improving therapeutic outcomes, and many machine learning models have been proposed to identify potential drug combinations. Recently, there has been a growing emphasis on enhancing the interpretability of machine learning models to improve our biological understanding of the drug mechanisms underlying the predictions. In this study, we developed a random forest model using simulated protein activities derived from Boolean modeling of breast cancer signaling pathways as input features. The model demonstrates a moderate Pearson's correlation coefficient of 0.40 between the predicted and experimentally observed synergistic scores, with the area under the curve (AUC) of 0.67. Despite its moderate performance, the model offers insights into the interpretable mechanisms behind its predictions. The model's input features consist solely of the individual protein activities simulated in response to drug treatments. Therefore, the framework allows for the analysis of each protein's contribution to the synergy level of each drug pair, enabling a direct interpretation of the drugs' actions on the signaling networks of breast cancer. We demonstrated the interpretability of our approach by identifying proteins responsible for drug resistance and sensitivity in specific cell lines. For example, the analysis revealed that the combination of MEK and STAT3 inhibitors exhibits only a moderate synergistic effect on MDA-MB-468 due to the negative contributions of mTORC1 and NF-κB that diminish the efficacy of the drug pair. The model further predicted that hyperactive PTEN would sensitize the cells to the drug pair. Our framework enhances the understanding of drug mechanisms at the level of the signaling pathways, potentially leading to more effective treatment designs.

Keywords Breast cancer, Drug resistance, Drug combinations, Machine learning, Signaling pathways

Breast cancer is a significant cause of death among women around the world, with approximately 2.2 million new cases and around 685,000 deaths in 2020[1]. Breast cancer systemic treatments like endocrine therapy, chemotherapy, and immunotherapy have shown promising results for patients[2]. However, treatment failure

[1]Bioinformatics and Systems Biology Program, School of Bioresources and Technology, King Mongkut's University of Technology Thonburi, Bangkok 10150, Thailand. [2]School of Information Technology, King Mongkut's University of Technology Thonburi, Bangkok 10140, Thailand. [3]Biotechnology Program, School of Bioresources and Technology, King Mongkut's University of Technology Thonburi, Bangkok 10150, Thailand. [4]Systems Biology and Bioinformatics Research Group, Pilot Plant Development and Training Institute, King Mongkut's University of Technology Thonburi, Bangkok 10150, Thailand. [5]Learning Institute, King Mongkut's University of Technology Thonburi, Bangkok 10140, Thailand. [6]Theoretical and Computational Physics Group, Center of Excellence in Theoretical and Computational Science, King Mongkut's University of Technology Thonburi, Bangkok 10140, Thailand. [7]Department of Physics, Faculty of Science, King Mongkut's University of Technology Thonburi, Bangkok 10140, Thailand. [8]National Nanotechnology Center (NANOTEC), National Science and Technology Development Agency (NSTDA), Pathum Thani 12120, Thailand. ✉email: teeraphan.lao@kmutt.ac.th

is still inevitable due to the dynamic nature of cancer cells that can persist under therapeutic pressure[3]. For instance, chemotherapy can induce drug resistance mutations[4], and the rapid rewiring of the signaling networks can diminish the effects of targeted therapies[5]. Recently, drug combination has demonstrated effectiveness for breast cancer treatment by mitigating drug resistance[6,7] and lowering dosage requirements[8–10]. However, it is unfeasible to investigate all possible drug pairs from a large space of small molecules despite having a high-throughput assay for drug combination screening[11]. Therefore, computational approaches play a crucial role in discovering effective drug combinations.

Many computational methods have been developed to predict the synergistic effects of drug combinations, ranging from traditional machine learning to deep learning models. The majority of traditional machine learning models for drug synergy prediction were implemented on the ensembled learning algorithm based on decision trees by integrating genomic information and drug features as input[12–15]. For example, Jeon et al.[13] developed extremely randomized trees using genomic information of the cancer cell lines, targets of drugs, and pharmacological information to predict drug synergy for 31 cell lines with Pearson's correlation coefficient of 0.74 between model predictions and observed synergy scores of drug combinations. Li et al.[12] used the single-drug-response profile from gene expression and drug physiochemical properties as features of a random forest that achieved an AUC score of 0.89.

An early work of deep learning for drug synergy utilized drug structures and genomic information of cancer cell lines as input features[16]. Subsequent deep learning models applied dimensional reduction approaches, such as autoencoding[17], subnetwork embedding[18], and principal component analysis[19], to lower the feature numbers. Additionally, other types of features were utilized, e.g., global chromatin profile, methylation profile, protein–protein interactions, protein-metabolite interactions, drug-target protein interactions, and drug inhibitory profiles against key cancer-related proteins[20–22].

In addition, several graph neural networks (GNNs) have been developed to learn from graph-structured data that includes diverse types of drug and omics data[23–28]. For example, DrugFormer[25] combined a transformer encoder with a Graph Attention Network (GAT) to predict drug resistance at the single-cell level using scRNA-seq data. SynerGNet[24] integrated heterogeneous biological data, such as genetic mutations, differential gene expression, and drug-protein association scores, into a human protein–protein network and used graph convolutional modules to learn from the graph-based data. GraphSynergy[27] used a Graph Convolutional Network (GCN) to extract information from a protein–protein interaction network related to protein modules targeted by drug combinations. DeepDDS[28] utilized a GNN to extract information from drug molecular structures. DTSyn[23] used a GCN to extract features from drugs and employed dual transformer encoders to capture the relationships between chemical substructures and genes, and between chemical substructures and cell lines. It ultimately integrated these learned representations for synergy prediction. These models demonstrated the effectiveness of GNNs in capturing crucial structural and biological information relevant to predicting drug synergy.

Along with these works, several models have interpretable characteristics. For instance, tree-based models allow interpretable results by extracting feature importance[14] or identifying the synergistic rules from frequent decision paths[13]. Other studies[29,30] have proposed deep learning models with constrained layers based on signaling pathways, which enables the investigation of the importance of signaling pathways to the predictions. These interpretable approaches are categorized as global interpretability, which focuses on understanding a model's overall behavior across all samples in the dataset[31]. For instance, feature importance indicates the key features the model relies on for making predictions throughout the dataset.

In contrast, recent efforts have prioritized the development of methods for local interpretability. These methods aim to understand the reasoning behind a model's individual predictions by identifying the key factors that lead to each decision[31]. For example, XGDP[32] is a graph-based deep learning model that predicts drug sensitivity and reveals the mechanism by which drugs interact with their targets. The study demonstrated that local interpretability could be achieved using two deep learning interpretation methods, Integrated Gradients[33] and GNNExplainer[34], to identify functional substructures of drugs and important genes, respectively, that are strongly associated with the predicted response of particular cell lines to particular drugs. TreeCombo[35] used TreeSHAP to calculate the importance of features for individual predictions. The feature importance can be averaged across all predictions to obtain a global level of feature importance. GraphSynergy[27] utilized an attention mechanism to assign contribution weights to different proteins within the protein–protein interaction network to the predicted drug synergy for a given drug combination in a given cell line. Therefore, for a given drug pair and cell line, the attention mechanism highlights key proteins that are most important in determining the predicted synergy score. DTSyn[23] utilized transformer attention scores to identify genes that significantly interact with each drug pair in a specific cell line. This identification provides insights into possible mechanisms of drug actions. Another example is TranSynergy[36], employing a network propagation technique on a protein–protein interaction network to capture the effects of drugs on individual proteins. The study identified the key genes/proteins contributing to each prediction instance using a novel method called Shapley Additive Gene Set Enrichment Analysis (SA-GSEA). In Supplementary Table S1, we compare the interpretability characteristics and performance of recent machine learning models for predicting drug synergy in cancer.

Overall, recent model development is increasingly prioritizing interpretability to improve the practical application of machine learning predictions in drug combination studies and enhance our understanding of their mechanisms. In the current study, we have developed a locally interpretable machine learning model (i.e., the model provides an interpretable mechanism for each drug combination prediction). We input protein activities simulated from Boolean models of breast cancers' protein signaling pathways, perturbed by drug combination, into a random forest model. Several studies have demonstrated that the simulated protein activities from the Boolean modeling framework can capture cancer cell behaviors in response to the effects of drug combinations[37–42]. This study, which combines Boolean modeling simulations with the random forest algorithm,

offers two key benefits. First, Boolean modeling allows for the full integration of the drug combination effect and cell line information into the simulation of cancer cells' dynamic protein activities. Second, the random forest algorithm selects the most relevant simulated protein activities to predict drug synergy, providing a deeper understanding of the model's decision-making process. As input features of the model are activities of individual proteins in response to drug treatments, the framework allows the interpretation of the prediction directly through the contribution of each protein toward the predicted synergy level of each drug pair. We demonstrate the interpretability of our approach by predicting the potential mechanisms of selected drug combinations and identifying perturbations to the genetics of cell lines (e.g., gain-of-function or loss-of-function mutations) that potentially contribute to resistance and sensitivity to the drug combinations.

Methods

The workflow of this study is outlined in Fig. 1. First, we simulated activities of 117 proteins in response to 574 drug pairs using a Boolean modeling framework from our previous study[41] (Fig. 1A). Then, the simulated steady-state protein activities were used as input features for constructing a random forest model to predict drug synergy (Fig. 1B). In addition, the framework provides two levels of interpretability: (1) global interpretation by feature importance and the accumulated local effects (ALE) of the features and (2) local interpretation by decomposing contribution of individual protein activities to each synergy prediction (Fig. 1C). We demonstrate the interpretability of our framework by predicting the potential pharmacological mechanisms of two chosen drug combinations and examining how abnormal protein activities in cell lines affect their resistance or sensitivity to these drug pairs.

Dataset

We selected 36 cancer drugs with known protein targets to investigate in this study (Table 1). Then, a drug combination dataset from the DrugComb database, version 1.5 (https://drugcomb.fimm.fi/), was retrieved. From the dataset, we identified 1139 drug pairs that are combinations of the 36 drugs tested on five selected breast cancer cell lines (MCF-7, T-47D, BT-549, MDA-MB-231, and MDA-MB-468). The selected cell lines are commonly used in breast cancer research to represent molecular subtypes of ER-positive (MCF-7 and T-47D)

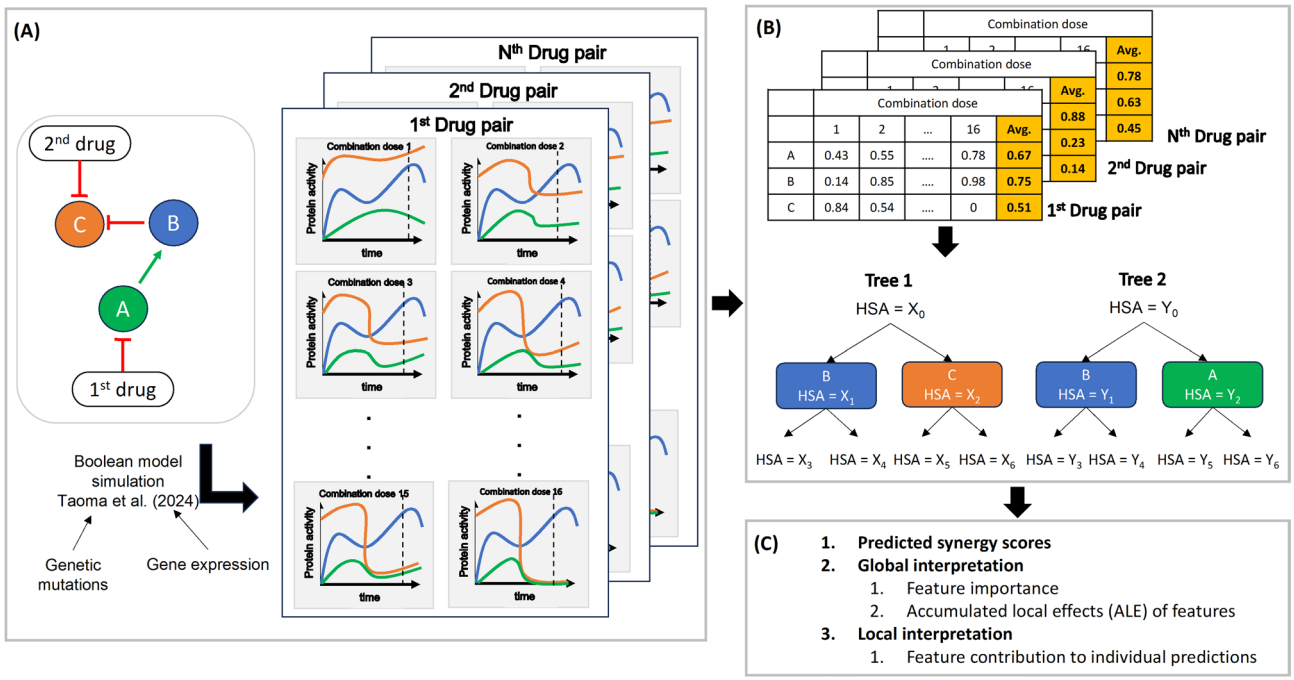

Fig. 1. The workflow for developing the random forest model using the simulation results of Boolean modeling as input features. (**A**) The breast cancer-related signaling network of 117 proteins was reconstructed using information from multiple databases. The red lines with a blunt end and the green line with a barbed end represent inhibitory and activatory interactions, respectively. The perturbation effect of drug pairs on the protein activities in the network was simulated using the Boolean modeling framework with cell line information (genetic mutations and gene expression). (**B**) The simulated protein activities at the steady state across 16 combination doses were averaged to generate the input features for the random forest model. The input is a 117-dimensional vector, with each element having a value ranging from 0 to 1 and representing the activity of a protein perturbed by a pair of drugs. (**C**) The random forest model predicts the HSA synergy scores for drug combinations retrieved from the DrugComb database. In addition, the model provides two levels of interpretability: (1) global interpretation by feature importance and the accumulated local effects (ALE) of the features and (2) local interpretation by decomposing the contribution of individual protein activities to each synergy prediction.

Drug	Drug target proteins (Asterisks indicate an agonistic effect; Non-asterisks indicate an antagonistic effect)
391210-10-9, Selumetinib, Trametinib	MEK1, MEK2
Dactolisib, PF-04691502	PI3K, mTORC1, mTORC2
Alpelisib, Buparlisib	PI3K
Antibiotic AY 22989, Deforolimus, NSC733504, Temsirolimus	mTORC1
AZD2014 (Vistusertib)	mTORC1, mTORC2
AZD5363 (Capivasertib), Enzastaurin, MK-2206	AKT
Celecoxib	PDPK1
Dasatinib	SRC, LCK, ABL1, ABL2
Emcyt, Mitotane, Raloxifene	ESR1*
Erlotinib hydrochloride, Gefitinib, Vandetanib	EGFR
Fulvestrant	ESR1
Imatinib, Nilotinib	ABL1
Lapatinib	EGFR, HER2
Megestrol acetate	PGR*
Paclitaxel	BCL2
Ruxolitinib	JAK2
Sapitinib	HER2
Sorafenib	EGFR, RAF1
Stattic	STAT3
Tamoxifen citrate	ESR1, MAPK8*
Trisenox	JUN*, CCND1, MAPK3*, MAPK1*, AKT1*
Geldanamycin	HSP90AA1

Table 1. The list of drugs included in this study and their respective target proteins identified from DrugBank and Therapeutic Target Database.

and triple-negative (BT-549, MDA-MB-231, and MDA-MB-468) cancer. We further removed drug pairs with identical drug targets, and 574 drug pairs remained for model training (Supplementary File S1).

The Highest Single Agent (HSA) scores associated with each drug pair in the DrugComb database were used as a labeled synergy score to train the model. HSA measures the deviation of the drug combination effects from the highest effect of single agents in pairs[43]. The distribution of HSA of the 574 drug pairs has a mean and standard deviation of 1.11 and 6.55, respectively (Supplementary Fig. S1). Positive and negative values of HSA indicate synergistic and antagonistic effects, respectively.

Simulated protein activities from Boolean modeling as the input features of the random forest model

The features of the random forest model for drug synergy prediction were extracted from the simulations of our previous Boolean models of breast cancer signaling pathways comprising 117 proteins[41]. The network was reconstructed based on information retrieved from KEGG[44,45] with additional proteins and regulatory interactions from the SIGNOR and SignaLink databases. The network was translated into 117 Boolean functions that encapsulate the regulatory interactions among genes/proteins in the network. Five versions of the model represent five selected breast cancer cell lines. To simulate the effects of drug pairs on the network, we first identified protein targets of the 36 unique drugs in our dataset (Table 1). Then, the effect of each drug pair was simulated by fixing the Boolean values of the target proteins to 0 or 1 (depending on whether the drug is an antagonist or agonist), and the Boolean functions were updated until the protein activities reached a steady state. Multiple repeats of an asynchronous update scheme were implemented, and the average Boolean values were calculated to represent the steady-state activity of each protein (value ranging between 0 and 1). Sixteen different drug combination doses were considered. The doses represent the probability of the target-protein nodes being 0 ("off") or 1 ("on") (depending on whether the drug is an antagonist or agonist) at the time the drug is applied to the model in each simulation repeat. The average protein activities at the steady state across the 16 combination doses were used as an input for the random forest. The input feature is a 117-dimensional vector, with each element having a value between 0 and 1, representing the activity of a protein perturbed by a pair of drugs.

The random forest model

The regression random forest was implemented with the scikit-learn package with the input features as the simulated activities of 117 proteins in response to drug pairs from Boolean modeling, while the labeled output is the HSA scores of the corresponding drug pairs. We used a stratified nested 5×5-fold cross-validation to identify the optimal hyperparameter set among 108 combinations (Table 2) using the GridSearchCV function from the scikit-learn package. Two levels of stratification were applied in the cross-validation, including five cell lines as the first level and the synergistic effect (negative or positive HSA scores) as the second level.

To obtain the optimal hyperparameter set, the whole dataset was split into five outer folds, each consisting of a training fold (e.g., Fig. 2A, box with green border) and a testing fold (e.g., Fig. 2A, box with red border).

Hyperparameter	Varied values	Hyperparameter	Varied values
max_depth	3, 4, 5	min_sample_leaf	8, 16, 24
max_sample	0.5, 0.7	min_sample_split	16, 24, 32
ccp_alpha	0.5, 0.7		

Table 2. Hyperparameters of random forests.

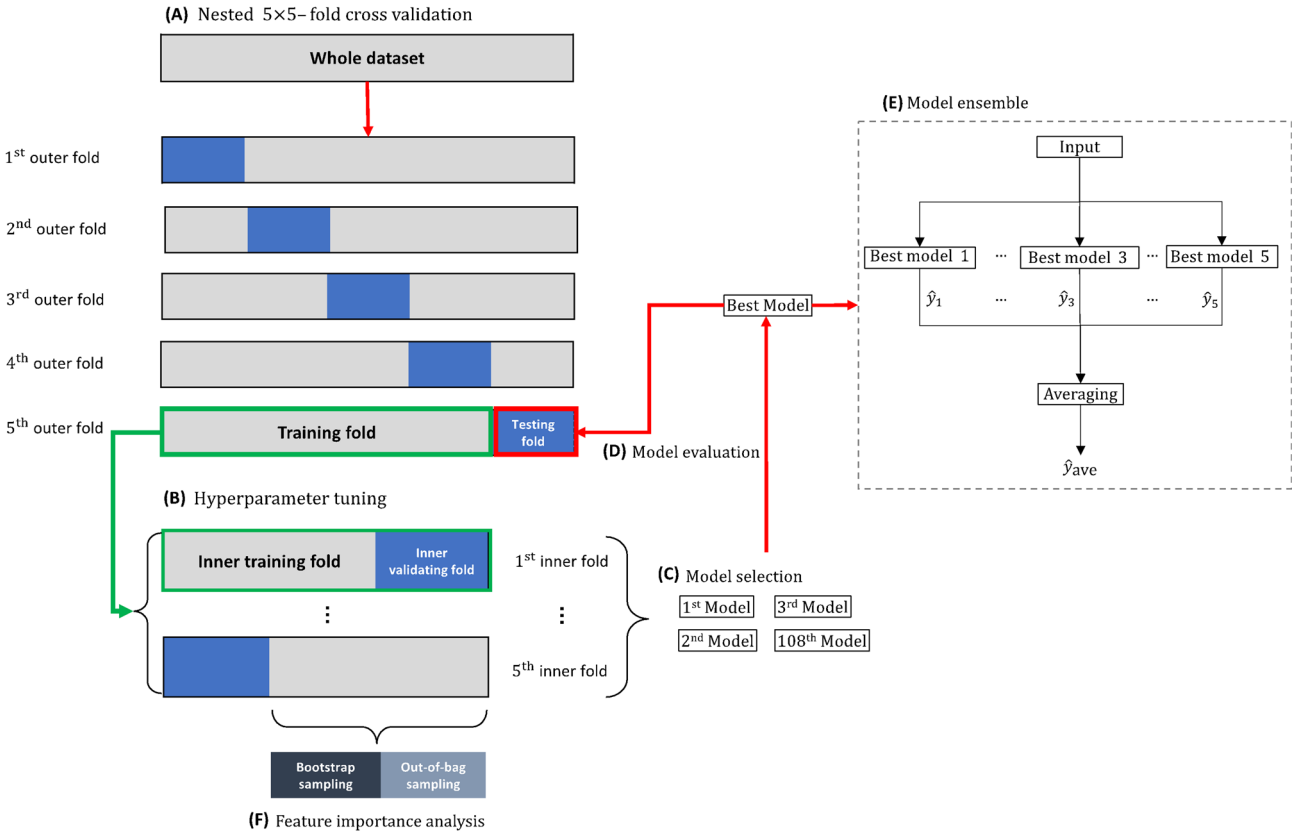

Fig. 2. The stratified nested 5 × 5-fold cross-validation for model development and an ensemble of the best models. (**A**) Splitting the whole dataset into outer training folds (e.g., the box with green border) and outer testing folds (e.g., the box with red border). (**B**) Splitting an outer training fold into inner training folds and inner validating folds for hyperparameter tuning with the bootstrap sampling by grid search. (**C**) Model selection from 108 hyperparameter sets. (**D**) Evaluation of the best model on the outer testing fold. (**E**) An ensemble of the best models from the five folds, where $\widehat{y}_n$ represent the prediction from each model and $\widehat{y}_{\text{ave}}$ is the final prediction, which is an average of the predictions made by the five models. (**F**) Feature importance analysis on out-of-bag samples.

Each outer training fold was further split into five inner folds for hyperparameter tunning (Fig. 2B). Each of 108 possible hyperparameter sets was used to train a model with the bootstrap sampling in the inner training fold. The models were evaluated with the inner validating fold, and the optimal set was identified based on the highest Pearson's correlation coefficient, averaged among the five inner folds, between model predictions and observed HSA scores (Fig. 2C). The model was then assessed with the outer testing fold (Fig. 2D). Finally, the five best models from the five outer folds were ensembled, and the predicted synergy scores from each model were averaged as the final predicted synergy score (Fig. 2E).

Global interpretation of the model

Next, we analyzed feature importance and the accumulated local effects (ALE) of the features to achieve the global interpretation of the model. The features from out-of-bag samples (i.e., the subset of training samples that are excluded during model training) in the inner fold (Fig. 2F) were permuted during the stratified nested 5 × 5-fold cross-validation using the rfpimp package (https://github.com/parrt/random-forest-importances/) to extract the important features. The importance score was calculated as the difference in the coefficient of determination between the baseline and permutation performance, where the larger reduction from the baseline indicates the greater importance of the features. The importance score of each feature is the average value across

the nested 5 × 5-fold. In addition, the contribution of protein activities to the synergistic score was investigated using the accumulated local effects (ALE)[46]. The approach measures the influence of each feature (each protein activity simulated from Boolean modeling) on the target variable (the synergy score). ALE divides the protein activities into multiple intervals based on their distribution, requiring finer intervals for regions with higher density. This allows for the calculation of the difference in synergy scores between the lower and upper limits in each interval before averaging these differences to estimate the pure effect of a single protein activity on the predicted HSA.

Local interpretation of the model

To explain the model's decision-making of individual predicted synergy scores, we extracted the contribution of each protein to the predicted value of HSA using the TreeInterpreter package (https://github.com/andosa/treeinterpreter). From this analysis, each prediction can be decomposed as.

$$HSA\left(x\right) = HSA_0 + \sum_{j=1}^{J} HSA_j\left(x\right), \tag{1}$$

where HSA_0 is the HSA value at the root of the tree, $HSA_j(x)$ is the contribution from protein j in the input protein activity vector x, and J is the total number of protein features ($J = 117$). Then, the contribution of protein j to the predicted HSA was averaged over all trees in the forest:

$$f_j\left(x\right) = \frac{1}{K} \cdot \sum_{k=1}^{K} HSA_{j,k}\left(x\right), \tag{2}$$

where $HSA_{j,k}(x)$ is the contribution from protein j in the input protein activity vector x from decision tree k and K is the total number of trees in the forest. Finally, the protein contribution to the HSA from each forest m was averaged over five random forest models

$$F_j\left(x\right) = \frac{1}{M} \cdot \sum_{m=1}^{M} f_{j,m}\left(x\right), \tag{3}$$

where $M = 5$.

Investigation of the effect of protein activities on the synergy of drug pairs

Aberrant protein activities can result in drug resistance or sensitivity in cancer cells. Understanding the molecular mechanisms behind these phenomena is essential to developing more efficient approaches for treating cancer. We investigated the effects of aberrant protein activities (for example, as a result of gain-of-function or loss-of-function mutations) on the synergy of drug pairs in five breast cancer cell lines. We selected three genes (P53, PTEN, and HRAS) to investigate as they have the highest frequencies of damaging mutations as observed from the DepMap database (Supplementary Fig. S2). For each cell line, we simulated both loss-of-function and gain-of-function scenarios for each gene. All the simulations of the aberrant activities were implemented with the same pipeline as described above, except that the protein activities of loss-of-function and gain-of-function genes were fixed at 0 and 1, respectively. The aberrations that increase or decrease the predicted HSA the most compared to the parental cell lines were further investigated in detail.

Results

Protein activities simulated from Boolean modeling of breast cancer signaling pathways

We simulated protein activities of 117 proteins in response to 574 drug combinations using our Boolean models of breast cancer signaling pathways. As an example, Fig. 3 shows the activities of selected proteins perturbed by the effects of drug pair AZD5363 (AKT inhibitor) and fulvestrant (ESR1 inhibitor) with 16 dose combinations in MCF-7. In the absence of both drugs (0 vs. 0), the levels of ESR1 and PI3K proteins are highly active, which is consistent with the behavior of the unperturbed MCF-7 cell line[47,48], whereas GATA3 is absent due to the loss of function in MCF-7[49].

When only AZD5363 (AKT inhibitor) is applied, the activities of AKT gradually reduce as the drug's dose increases from low to high (0.25 vs. 0, 0.75 vs. 0, to 1.0 vs. 0). At high doses of AZD5363 (e.g., 0.75 vs. 0 and 1 vs. 0), negative regulation of AKT on FOXO3 is relieved, resulting in the upregulation of FOXO3, ESR1, and CYCLIN D (AKT —| FOXO3 → ESR1 → CYCLIN D), which indicates a resistance mechanism that sustains the proliferation of the MCF-7 cells. When both AZD5363 and fulvestrant (ESR1 inhibitor) are administered together at high doses (e.g., 0.75 vs. 0.75 and 1 vs. 1), the drug resistance mechanism is mitigated (AKT, ESR1, and CYCLIN D activities are all low). The synergy of the drug pair was previously validated in experiment[50].

To utilize the simulated protein activities as the features in the random forest model, we averaged the protein activities at the steady state (vertical black-dashed lines in Fig. 3) from all 16 dose combinations. This resulted in a vector of size = 117 as the input for the random forest model, where each vector element represents the average activity at the steady state of a protein as perturbed by a drug pair. Although the information contained in the features is significantly compressed compared to the original time-series data (as shown in Fig. 3), we observed a modest correlation (absolute Pearson's correlation coefficients above 0.2) between the activities of several proteins and the HSA scores, as depicted in Fig. 4. In addition, the activities of most oncogenic proteins (orange

Fig. 3. The simulation of the perturbation effects of AZD5363 and fulvestrant on the MCF-7 cell line. Vertical blue-dashed lines indicate the time the drug combination is applied. Vertical black-dashed lines represent the new steady-state protein activities of the perturbed cells.

bars in Fig. 4) show a negative correlation with HSA, while tumor suppressor proteins (grey bars in Fig. 4) often show a positive correlation. This suggests that the features reflect the expected roles of the proteins—higher activities of oncogenic and tumor-suppressor proteins result in lower and higher synergy scores, respectively. This leads us to investigate the use of a random forest model, which utilizes the combined information from multiple proteins to predict the synergy scores, in the next step.

Development and performance of the random forest model

We used the activities of 117 proteins perturbed by drug pairs as the input to construct the random forest model. With stratified nested 5×5-fold cross-validation, we obtained five sets of optimal hyperparameters from each outer fold in Table 3. Five models, each trained with each of the optimal sets of hyperparameters, were finally assembled, where the predictions from the five models were averaged as the final predicted HSA score.

The model performance on the testing dataset achieves an average Pearson correlation of 0.40 and a mean squared error of 36.33 in the regression mode (Table 3). For the classification mode (drug pairs with an HSA above zero were classified as having a synergistic effect; otherwise, they were classified to have an antagonistic effect), the model exhibits an averaged AUC of 0.67 (Table 3). The full performance report can be found in Supplementary Table S2, where the model predicts drug pairs with synergistic effects better than the other class, indicated by a strong sensitivity of 0.81 with a low false negative rate of 0.18. The poor performance of predicting drug pairs with antagonistic effects is shown by the specificity of 0.39 and the false positive rate (FPR) of 0.60. Although the weak performance on predicting antagonistic drug pairs is observed, the model has a reliable performance on an unseen dataset with no statistical difference between the validating fold and the test fold (Wilcoxon signed rank-sum test, p-value > 0.05) in all performance metrics despite a slight overfit in the training dataset (Supplementary Table S2).

Feature importance and ALE analysis determining overall protein contribution to the synergy score (global interpretation of the model)

The importance scores of all proteins are calculated and provided in Supplementary Fig. S3. We discovered that the combined scores of the top 30 important proteins account for 98% of the total scores of all proteins.

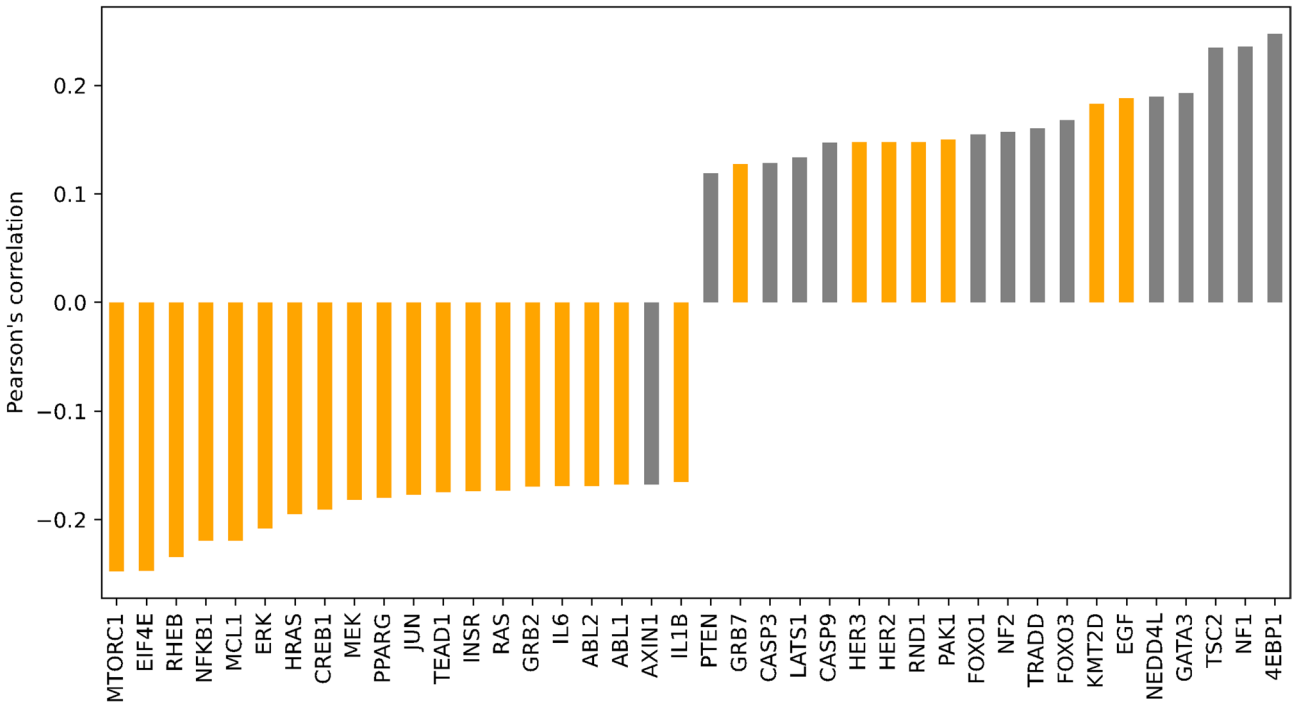

Fig. 4. Pearson's correlation coefficients between individual protein activities and the HSA scores. The colors grey and orange indicate tumor suppressor proteins and oncoproteins, respectively, as indicated by the OncoKB database and literature. Only the top 40 absolute values of correlation coefficients are displayed.

Model	Optimal hyperparameter set	Pearson's coefficient	Mean squared error (MSE)	Area under the curve (AUC)
1	max_depth = 4, max_sample = 0.7, min_sample_leaf = 16, min_sample_split = 32, ccp_alpha = 0.5	0.41	35.76	0.65
2	max_depth = 5, max_sample = 0.7, min_sample_leaf = 16, min_sample_split = 24, ccp_alpha = 0.5	0.47	30.61	0.72
3	max_depth = 5, max_sample = 0.7, min_sample_leaf = 16, min_sample_split = 16, ccp_alpha = 0.5	0.32	36.73	0.74
4	max_depth = 4, max_sample = 0.7, min_sample_leaf = 16, min_sample_split = 24, ccp_alpha = 0.7	0.46	39.17	0.62
5	max_depth = 3, max_sample = 0.7, min_sample_leaf = 16, min_sample_split = 32, ccp_alpha = 0.5	0.34	39.39	0.61
Average		0.4	36.33	0.67

Table 3. The optimal set of hyperparameters from stratified nested 5 × 5-fold cross-validation and the performance of the model on the testing fold.

Consequently, we selected these 30 top proteins (Fig. 5A) for further analysis. These proteins were further characterized into oncogenic and tumor suppressor protein types, as indicated by the OncoKB database and literature, and analyzed separately for enrichment. We found that the oncoproteins are significantly enriched in the mTOR signaling, endocrine resistance, and PI3K-AKT pathways. In contrast, tumor suppressor proteins are significantly enriched in the apoptosis, platinum drug resistance, and P53 signaling pathways. The complete list of enriched KEGG pathways[44,45] is shown in Supplementary Fig. S4.

Next, we conducted an ALE analysis to examine how the activity level of each protein affects the directional change of the synergistic HSA score (Supplementary File S2). Among the top 30 proteins ranked by importance scores and the absolute coefficients of ALE linear regression, 22 proteins are common to both methods, indicating their consistency. For 26 out of the top 30 proteins in Fig. 5A, the ALE analysis correctly demonstrates the relationship between the protein types (oncogenic or tumor suppressor protein) and the HSA level. In other words, the analysis predicts a decrease in HSA scores with increasing oncogenic protein activities (Fig. 5B) and an increase with rising tumor suppressor protein activities (Fig. 5C). The other four proteins out of the top 30, including KMT2D, RAF1, SOS1, and IGF1R, exhibit an inconsistent relationship (Supplementary Fig. S5), suggesting further revisions of the Boolean model are needed.

Our model captures a strong effect of the PGR protein that dramatically reduces the HSA score from 1.31 to − 2.51 as its activity increases (Fig. 5B). This explains why drugs combined with PGR agonists (e.g., megestrol acetate) were mainly predicted to have an antagonistic effect, which is consistent with the actual HSA

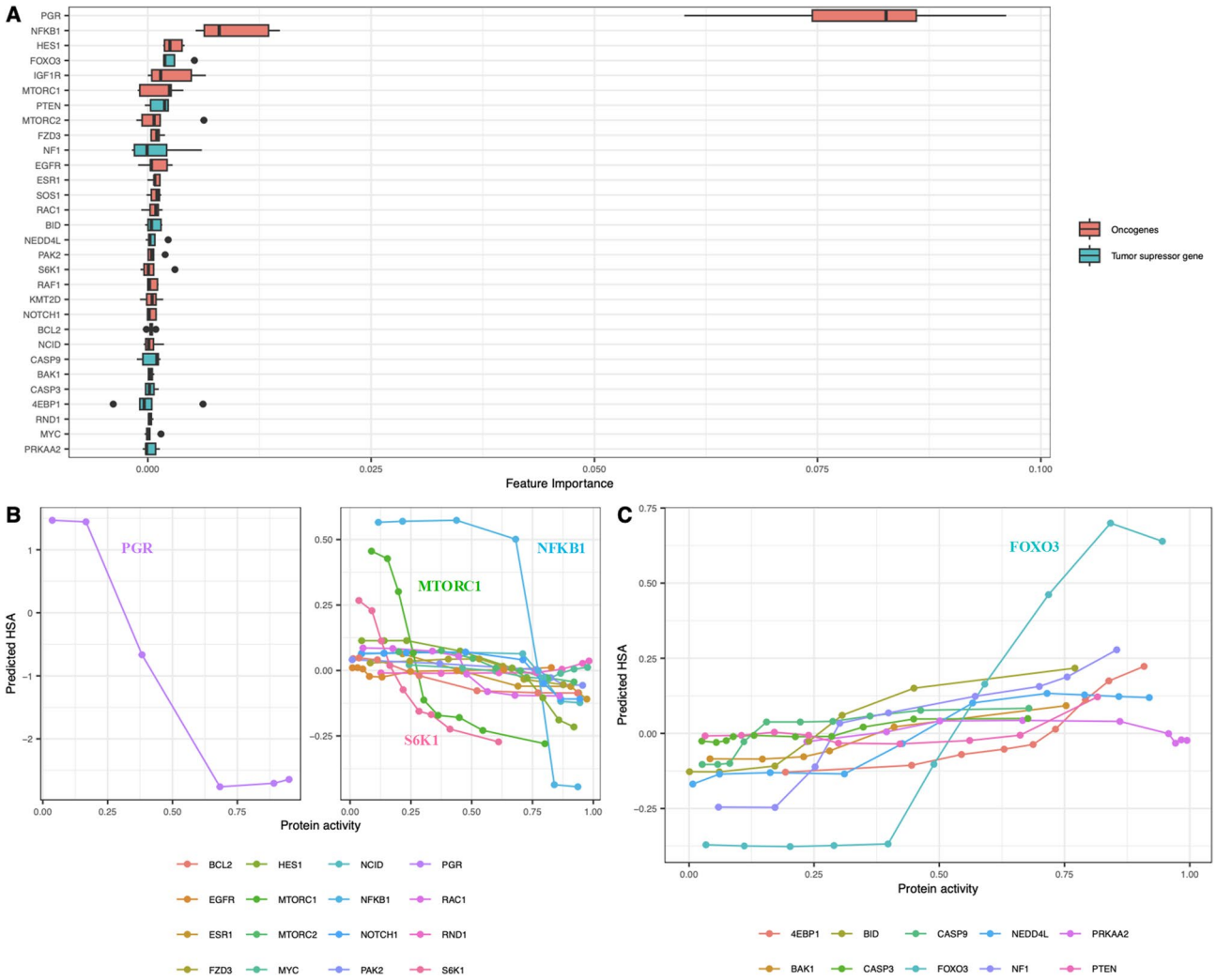

Fig. 5. Feature importance and the accumulated local effects (ALE) of the proteins. (**A**) Top 30 important proteins calculated from the out-of-bag data during the nested 5 × 5-fold cross-validation. (**B**) The ALE plot for oncoproteins. (**C**) The ALE plot for tumor suppressor proteins.

observed from the DrugComb database (Supplementary Fig. S6). Other oncoproteins significantly decreasing the HSA level include NF-κB, mTORC1, and S6K1 (NF-κB promotes proliferation, while mTORC1 and S6K1 stimulate protein synthesis). Our model predicts 43 out of 47 drug pairs that contain an mTORC1 inhibitor (e.g., ANTIBIOTIC AY 22989) as synergistic (Supplementary Fig. S6). For tumor suppressor proteins, a notable effect is observed in FOXO3, where the analysis indicates the largest HSA increase when the protein activity rises. In line with this, all 27 pairs of drugs in the dataset that contain an AKT inhibitor (such as MK-2206 or AZD5363), which subsequently activates FOXO3, are predicted to have a synergistic effect (Supplementary Fig. S6).

We further investigated why these 30 proteins are relevant in drug synergy prediction by classifying them into drug-target and non-drug-target proteins. Seven of the top 30 proteins are the direct target of the drugs used in this study. Analysis of protein activity from RNAseq data in the DepMap database revealed substantial upregulation of the seven proteins in the five selected cell lines compared to the other breast cancer cell lines (Supplementary Fig. S7). The other 23 non-drug target proteins are within the second neighbor of the drug target proteins, indicating their essential for predicting drug synergy as they receive signals propagated from drug target proteins[51].

Aberrant protein activities causing resistance or sensitivity to the synergy of drug pairs (local interpretation of the model)

Next, we implemented scenarios in which breast cancer cells have acquired aberrant protein activities (e.g., acquired additional gain-of-function or loss-of-function mutations) and studied their response to five pairs of drugs known to exhibit synergy in experimental studies (Table 4). For this task, we investigated proteins that are direct targets of the drug pairs. We also looked into the aberrant activities of three proteins (P53, PTEN, and HRAS), as their genes are most frequently mutated in breast cancer.

Table 4 displays the change in HSA (ΔHSA) between the strains with aberrant activities and the parental cell line computed by our random forest model. Among the aberrant strains, the gain-of-function (GoF) in the AKT protein to MCF-7 shows the largest HSA reduction (ΔHSA = − 3.74) when treated with AZD5363 + Fulvestrant. A similar decrease is also observed in the T-47D AKT-GoF cell line with ΔHSA of − 3.08. On the other hand, the GoF in PTEN to MDA-MB-468 treated with 391210-10-9 + Stattic shows the largest increase in HSA (ΔHSA = + 4.67). Additionally, the predictions indicate that the acquired loss-of-function (LoF) of PTEN has a significant impact on both luminal and triple-negative subtypes of breast cancer, as it diminishes the synergistic effect in most of the selected drug pairs.

Next, we conducted a local interpretability analysis to demonstrate how the decision-making process of HSA predictions was made in the strains with the largest deviation of ΔHSA from the parental cell lines (MCF-7 AKT-GoF treated with AZD5363 + Fulvestrant and MDA-MB-468 PTEN-GoF treated with 391210-10-9 + Stattic). To identify the individual proteins that significantly contributed to the change in HSA, we first calculated each protein's contribution to the synergy scores of both the parental and aberrant strains using Eq. (1)–(3). Next, we determined the difference between the contributions from the aberrant and the parental strains (ΔHSA) and ranked these differences (Supplementary File S3 and File S4). We then selected the top 10 proteins with the largest ΔHSA, focusing only on those with substantial changes in activity between the aberrant and the parental strains (i.e., with a ΔActivity from Boolean simulation greater than 0.1). This selection allows us to focus on proteins whose activity changes can be linked to specific interactions within our Boolean model, enabling us to interpret how these identified interactions drive the observed effects on drug synergy.

MCF-7 AKT-GoF treated with AZD5363 + fulvestrant

Figure 6 lists the top contributing proteins that help reveal the underlying mechanism of the large reduction in the HSA in MCF-7 AKT-GoF when treated with AZD5363 (AKT inhibitor) + Fulvestrant (ESR1 inhibitor).

The synergistic effect between AZD5363 and fulvestrant in the parental MCF-7 cell line is heavily contributed by FOXO3, mTORC1, and NF-κB, with the HSA contribution of 0.58, 0.56, and 0.41, respectively (blue solid bars in Fig. 6). In the presence of the GoF of AKT, FOXO3 is highly downregulated, while mTORC1 and NF-κB are highly upregulated (orange hatched bars in Fig. 6). These changes in protein activities caused by the excessive activity of AKT reduce the HSA contribution of the proteins to become highly negative (− 0.11, − 0.21, and − 0.29 for FOXO3, mTORC1, and NF-κB, respectively) (blue hatched bars in Fig. 6). The results suggest that these proteins and the associated pathways may play important roles in the resistance of MCF-7 AKT-GoF to the drug pair.

We propose the possible resistance mechanisms of the GoF cell line to the drug pair in Fig. 7 based on protein profiles from Fig. 6. The interactions depicted in Fig. 7 were obtained from our Boolean model[41], which compiled protein interactions from KEGG, SIGNOR, SignaLink, and relevant literature. The evidence supporting the interactions depicted in Fig. 7 is detailed in Supplementary Table S3. According to the Boolean model simulation, hyperactivity of AKT inhibits the activity of FOXO3 from 0.75 in the parental MCF-7 cells to 0 in the AKT-GoF variant (orange bars in Fig. 6). FOXO3 is recognized as a tumor-suppressor protein in breast cancer[57]. Research has shown that activating FOXO3 in MCF-7 cells inhibits their growth and induces apoptosis while down-regulating FOXO3 in these cells results in estrogen-independent growth[57,58]. This may explain the reduced synergistic effect of the drug combination in AKT-GoF MCF-7 cells.

Increased activity of AKT also enhances mTORC1, which subsequently suppresses 4EBP1 and activates EIF4E. Active mTORC1 also activates S6K1. The three proteins (4EBP1, EIF4E, and S6K1), which highly contribute to the reduction of HSA in Fig. 6, are involved in promoting protein synthesis[59].

Additionally, the profiles in Fig. 6 suggest four alternative AKT-induced proliferation pathways, including.

1. AKT → NF-κB → proliferation,
2. AKT → HES1 → proliferation,
3. AKT —| NF1 —| proliferation, and
4. AKT → PRKACA —| NEDD4L —| proliferation.

In our Boolean model, hyperactivity of AKT increases NF-κB activity by 0.4, contributing to ΔHSA of − 0.7. Consistently, evidence indicates that AKT activity is linked to NF-κB activity and endocrine resistance in ER + breast cancer[60,61]. Furthermore, AKT interacts with the Notch signaling pathway, leading to the activation of HES1, a downstream effector of cell fate regulation and proliferation[62]. Our simulation of AKT-GoF indicates that HES1 activity increased by 0.4, resulting in a ΔHSA of − 0.15. In addition, overactive AKT causes a reduction in the NF1 activity (ΔActivity = − 0.4). Loss of NF1 activity has been associated with endocrine resistance in ER + breast cancer[63]. Consistently, our prediction shows the HSA reduction (ΔHSA = − 0.2) contributed by down-regulating NF1. High activity of AKT also upregulates PRKACA (ΔActivity = + 0.75), leading to the reduction in the NEDD4L activity (ΔActivity = − 0.74), which contributes to the reduction in HSA (ΔHSA by PRKACA and NEDD4L = − 0.21 and − 0.18, respectively). NEDD4L serves primarily as a tumor-suppressor protein[64]. Overall, the GoF effect of the AKT protein helps MCF-7 escape death by negating the effect of AZD5363, reprogramming the activities of FOXO3, mTORC1, and NF-κB, among others, which stimulates protein synthesis and proliferation (Fig. 7).

It should be noted that IRS1 and SOS1, initially ranked 6th and 9th among the top contributing proteins, were removed from Fig. 6 due to their reduced activities in the AKT-GoF strain despite being classified as oncogenes. This reduction can be explained by the interactions described in our Boolean model. IRS1 is inhibited by S6K1[65], whose activity was upregulated in the AKT-GoF strain. Similarly, SOS1 is activated by IRS1 through GRB2[66]. Consequently, the reduced activity of IRS1 led to a decrease in SOS1 activity. Despite this, the reduced activity of the two oncoproteins (IRS1 and SOS1) decreased the synergistic score by 0.22 and 0.19, respectively, as predicted

Drug combination	Drugs' targets	Predicted HSA	Predicted HSA and ΔHSA (HSA of aberrant cell line—HSA of parental cell line) in parentheses									
			First drug's target		Second drug's target		P53		PTEN		HRAS	
			GoF	LoF	GoF	LoF	GoF	LoF	GoF	LoF	GoF	LoF
AZD5363 + Fulvestrant on MCF-7[50]	AKT and ESR1	3.31	− 0.43 (− 3.74)	4.64 (1.33)	2.72 (− 0.59)	2.22 (− 1.09)	3.13 (− 0.18)	2.98 (− 0.33)	5.73 (2.42)	2.63 (− 0.68)	3.65 (0.34)	3.05 (− 0.26)
AZD5363 + Fulvestrant on T-47D[50]	AKT and ESR1	3.66	0.58 (− 3.08)	4.49 (0.83)	4.40 (0.74)	4.63 (0.97)	3.93 (0.27)	3.66 (0*)	3.79 (0.13)	3.33 (− 0.33)	1.37 (− 2.29)	4.62 (0.96)
AZD2014 + Selumetinib on BT-549[52]**	mTORC1/2 and MEK	3.17	1.20 (− 1.97)	3.18 (0.01)	0.48 (− 2.69)	3.76 (0.59)	3.41 (0.24)	3.17 (0*)	3.18 (0.01)	3.17 (0*)	2.12 (− 1.05)	2.86 (− 0.31)
Gefitinib + AY22989 on MDA-MB-231[53]	EGFR and mTORC1	0.74	0.22 (− 0.52)	− 0.10 (− 0.84)	0.66 (− 0.08)	2.21 (1.47)	0.25 (− 0.49)	0.74 (0*)	0.21 (− 0.53)	0.36 (− 0.38)	0.44 (− 0.3)	− 0.38 (− 1.12)
391210-10-9 + Stattic on MDA-MB-468[54–56]***	MEK and STAT3	1.43	1.15 (− 0.28)	0.99 (− 0.44)	2.70 (1.27)	1.39 (− 0.04)	1.64 (0.21)	1.43 (0*)	6.10 (4.67)	0.71 (− 0.72)	1.17 (− 0.26)	1.63 (0.2)

Table 4. The predicted HSA of five drug pairs with different aberrant protein activity scenarios. *ΔHSA = 0 indicates that the cell lines already contain the respective mutations. **Carracedo et al.[52] investigated the synergy between rapamycin and UO126, which inhibit mTOR and MEK, respectively. ***The references examined the synergy between MEK and STAT3 inhibitors but in different types of cancer.

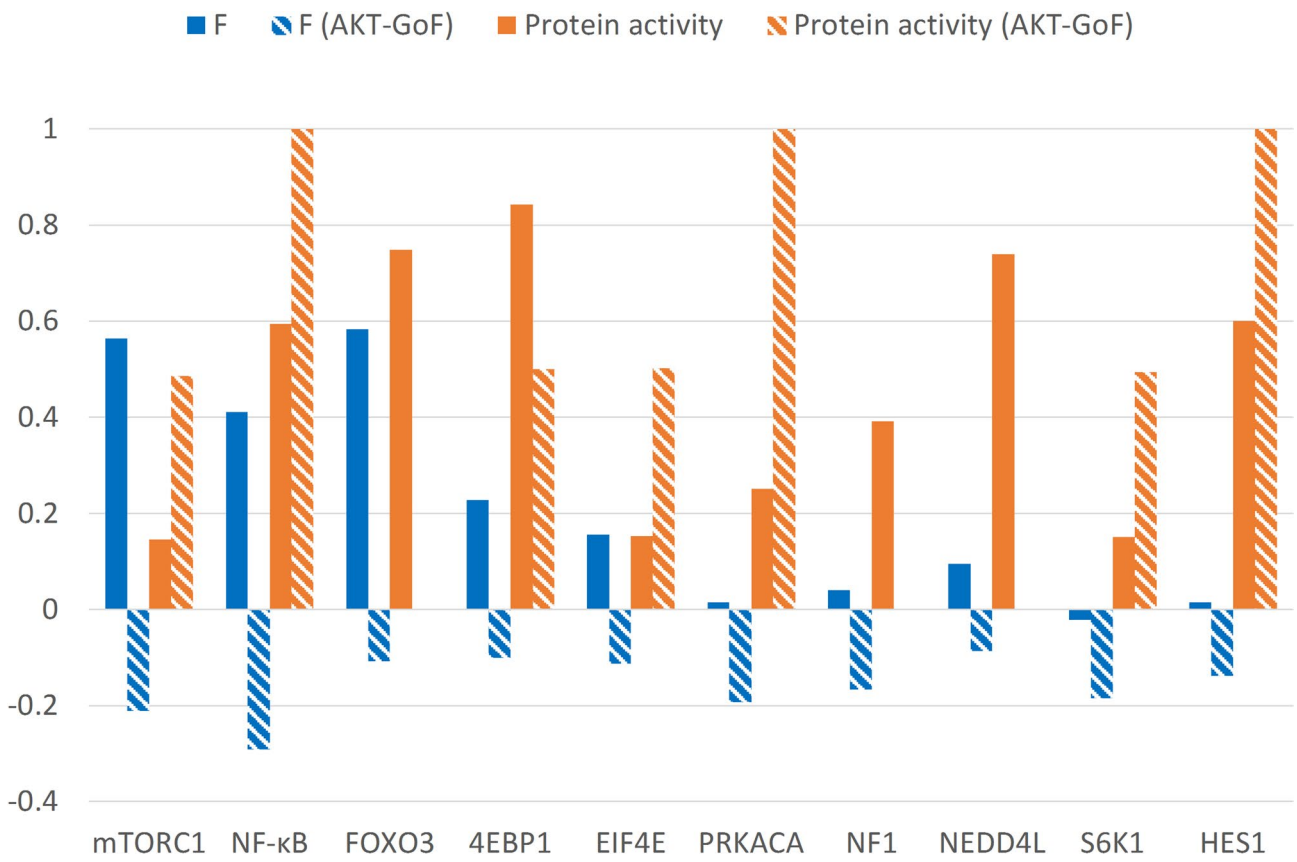

Fig. 6. Top 10 proteins that contribute to the largest reduction in the predicted HSA of MCF-7 AKT-GoF compared to the parental MCF-7 cell line. Blue bars display the HSA contributions from individual proteins (*F*) calculated according to Eq. (3). Orange bars display the activities of the respective proteins simulated from Boolean modeling. (Solid bars) Parental MCF-7. (Hatched bars) MCF-7 AKT-GoF.

by our random forest models. We could not reconcile this inconsistency and chose to include S6K1 and HES1, which were ranked 11th and 12th among the highest contributing proteins, in our analysis (Figs. 6 and 7) instead.

MDA-MB-468 PTEN-GoF treated with 391210-10-9 + Stattic

The combination of MEK and STAT3 inhibitors has been shown to exert a synergistic effect on several cancer types[54–56]. However, in MDA-MB-468, the drug pair 391210-10-9 (MEK inhibitor) + Stattic (STAT3 inhibitor) only moderately synergizes with HSA of 0.63, as reported in DrugComb, and 1.43, as predicted by our random forest model. The modest synergy can be explained by the negative HSA contributions from proteins such as mTORC1 and NF-κB that diminish the efficacy of the drug pair (blue solid bars in Fig. 8).

Our model predicts that the GoF mutation of PTEN (i.e., hyperactive PTEN) to MDA-MB-468 increases the sensitivity of the drug pair with ΔHSA = 4.67 (Table 4). When individual protein contributions are considered, the GoF of PTEN to the cell line causes an increase in the HSA contribution mainly from mTORC1 and NF-κB with ΔHSA of 0.83 and 0.70, respectively (blue hatched bars in Fig. 8). Predicted mechanisms explaining the sensitivity of MDA-MB-468 PTEN-GoF to MEK + STAT3 inhibitors are proposed in Fig. 9. Again, the interactions shown in Fig. 9 were obtained from our Boolean model, which was developed using protein interaction data from KEGG, SIGNOR, SignaLink, and relevant literature. Evidence supporting the interactions between proteins in the figure is listed in Supplementary Table S4.

When PTEN becomes constitutively active, it triggers a series of cascading effects. Firstly, in our Boolean model, AKT activates β-catenin (CTNNB1)[67], which can induce EGFR[68]. Therefore, hyperactive PTEN, which inhibits AKT, leads to a down-regulation of EGFR. Our simulation shows that EGFR activity decreases from 0.80 to 0.48 (orange bars in Fig. 8) under the condition of hyperactive PTEN. Since EGFR activates both MEK and STAT3, this reduction may help explain why hyperactive PTEN further enhances the synergistic effects of the drug pair. In addition, PTEN down-regulates MEK through the PIP3/RAS/RAF/MEK pathway[69,70]. Consistent with our prediction, previous studies have shown that PTEN induction sensitizes MDA-MB-468 cells to MEK inhibitors[71,72].

Secondly, in our simulation, PTEN downregulates AKT, leading to decreased levels of both NF-κB and HES1 through the Notch signaling pathway. HES1 is an important downstream effector in the Notch signaling pathway[73], which is essential for determining cell fate and regulating cell proliferation, while NF-κB serves as a key regulator of both proliferation[74–76] and apoptosis[77]. Research indicates that the AKT, Notch, and NF-

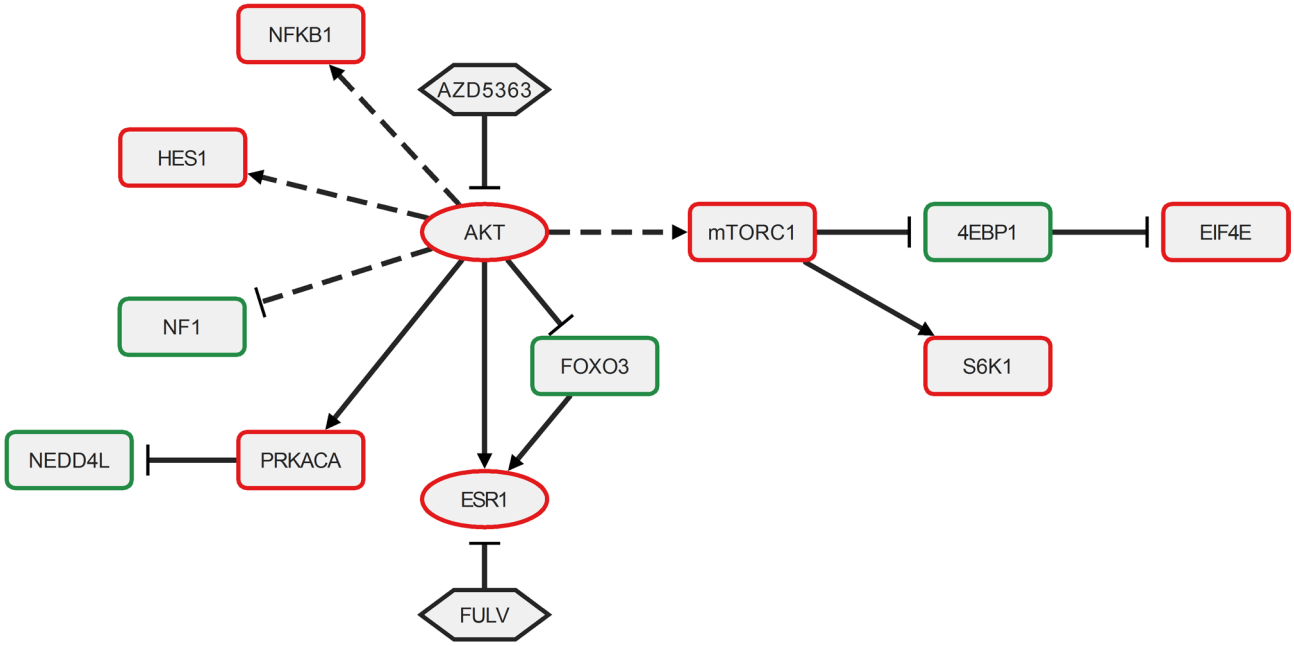

Fig. 7. The predicted resistance mechanisms of MCF-7 AKT-GoF to AKT and ESR1 inhibitors based on the top 10 contributing proteins (rectangle nodes) from Fig. 6. AKT and ESR1 (oval nodes) are not in the top 10 list but are included because they are direct targets of the drug pair (hexagon nodes). Red and green borders indicate oncoproteins and tumor-suppressor proteins, as indicated by the OncoKB database and literature. Arrows and lines with a blunt end represent activation and inhibition interactions, respectively. The interactions shown in the figure were retrieved from our Boolean model. Direct interactions between nodes, as determined in our Boolean model, are represented by solid lines. Interactions through intermediate proteins are represented by dashed lines. The evidence supporting these interactions is listed in Supplementary Table S3.

κB signaling pathways interact with one another and significantly influence cell proliferation in triple-negative breast cancer[78].

Thirdly, active PTEN reduces mTORC1 and mTORC2 activities by 0.62 and 0.58, respectively. The down-regulation of mTORC1 decreases protein translation by regulating 4EBP1, EIF4E, and S6K1, as discussed in the previous section. Furthermore, NEDD4L is negatively regulated by mTORC2 through SGK1[79]. NEDD4L primarily acts as a tumor-suppressor protein[64]. Hyperactive PTEN results in the inactivation of mTORC2, thereby enhancing the function of NEDD4L.

Discussion

Although dynamic models of signaling pathways of cancer are useful for investigating the mechanisms of drug synergy[37–42], the predictive power of these models is outperformed by machine learning models. To address this problem, we integrated a random forest model with the simulated protein activities from Boolean modeling to predict drug synergy in breast cancer. We used the TreeInterpreter package to enable our hybrid model to investigate the contribution of the individual proteins to the predicted value of synergy scores. This offers a more detailed understanding of the mechanism underlying the drug combination, as the contribution of individual proteins can be directly analyzed. Also, the effect of aberrant protein activities (e.g., due to acquired mutations) of the cell lines can be predicted as their effects can be simulated directly in our Boolean modeling framework. It is important to understand such perturbations in breast cancer cells as they can affect the effectiveness of many drugs. For example, luminal breast cancer cells with constitutively active AKT resist the drugs BYL719 and GDC0941[80]. Furthermore, a phase II clinical trial revealed potential resistance to MK-2206 due to AKT mutations or PTEN loss[81]. Additionally, the loss of function of the RB1 protein impacts the effectiveness of CDK4/6 inhibitors in treating ER + /HER2 – metastatic breast cancer[82].

By combining mechanistic modeling with random forest, we identified important proteins that influence the synergistic effect in breast cancer with the quantitative interpretation of the protein activities with respect to the synergy scores. The interpretation can serve as a valuable guide to design treatment actions towards these proteins to enhance the synergistic effect. For example, PGR was predicted as an important protein (Fig. 5A) with a sharp decrease in HSA when the protein activity increases (Fig. 5B). With this information, one may reduce its activities in order to promote the synergistic effect of drug pairs.

Our study also revealed the effects of aberrant protein activities on the resistance and sensitivity of drug combinations in five breast cancer cell lines. We highlight the GoF of AKT that can greatly impact the synergy score of AZD5363 and fulvestrant in MCF-7 by counteracting the synergistic to antagonistic effect, whereas the GoF of PTEN can sensitize the MDA-MB-468 cells to drug combination between 391210-10-9 and Stattic. In addition, we demonstrated that the acquired loss-of-function of PTEN has a substantial impact on both luminal

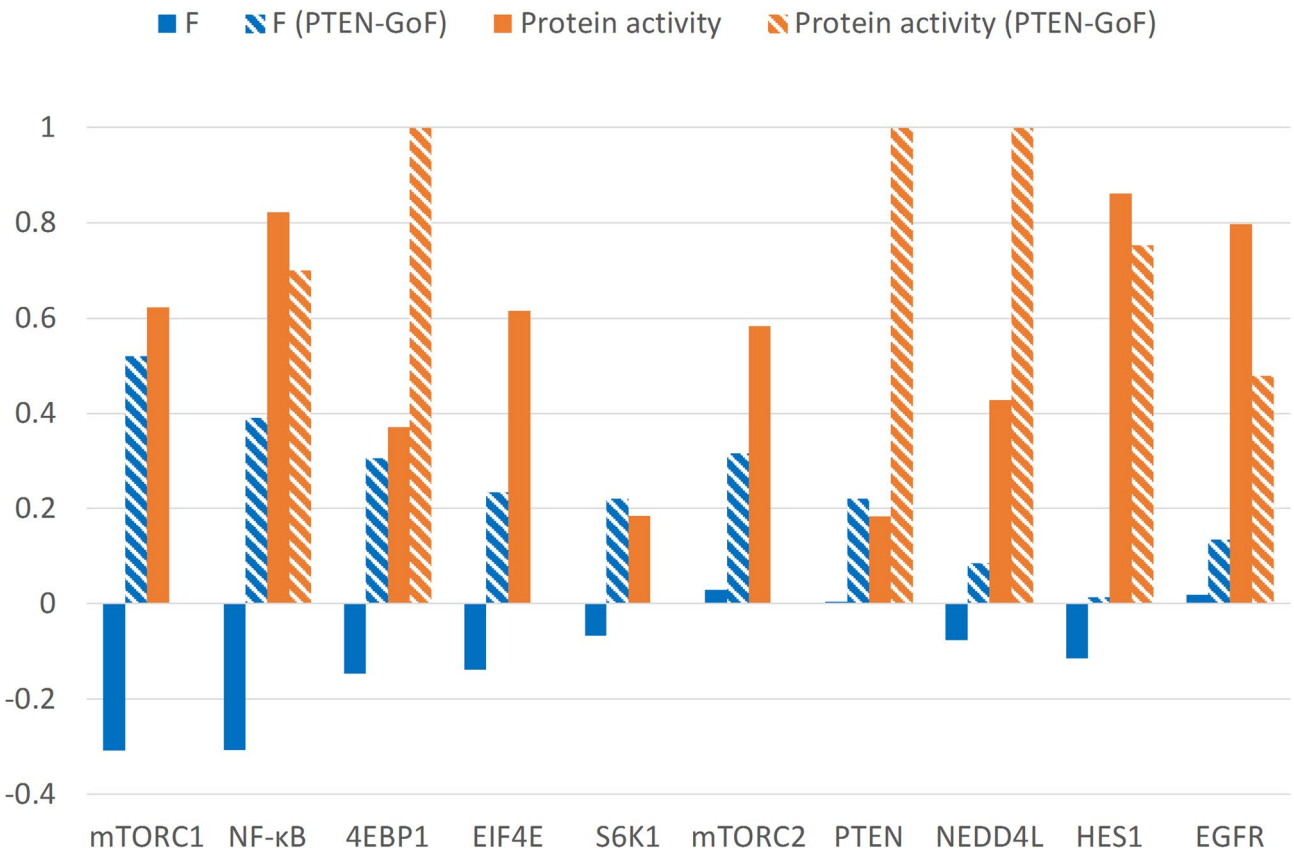

Fig. 8. Top 10 proteins that contribute to the largest increase in the predicted HSA of MDA-MB-468 PTEN-GoF compared to the parental MDA-MB-468 cell line. Blue bars display the HSA contributions from individual proteins (*F*) calculated according to Eq. 3. Orange bars display the activities of the respective proteins simulated from Boolean modeling. (Solid bars) Parental MDA-MB-468. (Hatched bars) MDA-MB-468 PTEN-GoF.

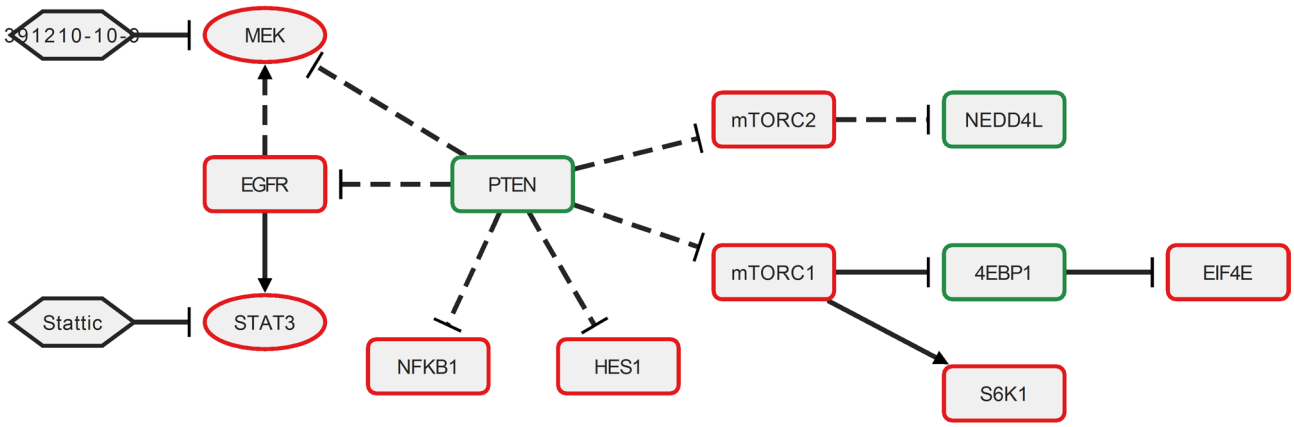

Fig. 9. The predicted sensitivity mechanisms of MDA-MB-468 PTEN-GoF to MEK and STAT3 inhibitors based on the top contributing proteins (rectangle nodes) from Fig. 8. STAT3 and MEK (oval nodes) are not in the top 10 list but are included because they are direct targets of the drug pair (hexagon nodes). Red and green borders indicate oncoproteins and tumor-suppressor proteins, as indicated by the OncoKB database and literature. Arrows and lines with a blunt end represent activation and inhibition interactions, respectively. The interactions shown in the figure were retrieved from our Boolean model. Direct interactions between nodes, as determined in our Boolean model, are represented by solid lines. Interactions through intermediate proteins are represented by dashed lines. The evidence supporting these interactions is listed in Supplementary Table S4.

and triple-negative breast cancer subtypes, as it was predicted to reduce the synergistic effect of several drug combinations.

Our model achieves a moderate Pearson's correlation of 0.40 and the area under the curve (AUC) of 0.67. However, the interpretable property of our framework outweighs this drawback by providing insight into the underlying mechanism of each drug combination. The rationale for using interpretable features in our work closely resembles TranSynergy. In the work, each feature corresponds to a single gene/protein, enabling direct interpretation of the features that contribute to each synergy prediction instance. TranSynergy encoded the effects of drugs on proteins by propagating information from drug targets on a protein–protein interaction network, while our current framework simulated protein activities in response to drug combination perturbations in the dynamic signaling networks of breast cancer cells. Our simulation fully integrated the cell line's genetic and expression profiles within the Boolean modeling framework[41].

Based on the cell lines studied in our current work and those analyzed by TranSynergy, T-47D is a common overlap. Therefore, we examine the list of highly influential proteins identified by each method. Using the drug combination between BEZ-235 and erlotinib in T-47D as an example, seven of our positive contributing proteins overlap with top genes that have the highest SHAP values identified by TranSynergy. These proteins include CDK4, AKT1, AKT3, EGFR, NF2, STK11, and ESR1 (see Fig. S4 in the TranSynergy paper[36]). Additionally, the top 20 protein contributors identified by our model that do not overlap with TranSynergy are shown in Supplementary Fig. S8. These contributors are enriched in the MAPK signaling pathway (Supplementary Fig. S9), which is downstream of the PI3K/AKT/mTOR and EGFR pathways that are inhibited by BEZ-235 and erlotinib, respectively. Identifying the MAPK signaling pathway as an enriched pathway perturbed by the drug pair in T-47D is consistent with the analysis by TranSynergy.

Although the interpretability of our approach is promising, the model exhibits only a moderate performance. We believe this could be enhanced by expanding the protein signaling network and refining the interactions between the proteins. It was previously shown that extending networks could improve the model performance of drug synergy prediction in various subtypes of breast cancers[42].

In the current framework, the hyperparameter optimization of the model was tuned based on 5×5-fold nested cross-validation to obtain a reliable model from the small training dataset. The number of ensembled models was obtained from the number of outer folds in nested cross-validation. We show that the number of ensembled models has an insignificant impact on the model performance (Supplementary Fig. S10), demonstrating the robustness of the framework, even with a limited training dataset. However, using a larger training dataset is recommended to enhance the model's performance.

Despite the limitations mentioned above, our model, with the capability to directly interpret drug combination action in the breast cancer cell lines through individual protein information, can enhance the understanding of drug mechanisms at the level of the signaling pathways, potentially leading to more effective treatment designs.

Data availability

The model and related data are available on GitHub: https://github.com/Ktaoma/LogicForests.

Received: 7 January 2025; Accepted: 13 May 2025
Published online: 22 May 2025

References

1. Ferlay, J. *et al.* Global cancer observatory: cancer today. *International Agency for Research on Cancer* https://gco.iarc.fr/today (2020).
2. Harbeck, N. et al. Breast cancer. *Nat. Rev. Dis. Primers* **5**, 66 (2019).
3. Vasan, N., Baselga, J. & Hyman, D. M. A view on drug resistance in cancer. *Nature* **575**, 299–309 (2019).
4. Johnson, B. E. et al. Mutational analysis reveals the origin and therapy-driven evolution of recurrent glioma. *Science* **343**, 189–193 (2014).
5. Bosch, A. et al. PI3K inhibition results in enhanced estrogen receptor function and dependence in hormone receptor-positive breast cancer. *Sci. Transl. Med.* **7**, 28351 (2015).
6. Xu, L. et al. A meta-analysis of combination therapy versus single-agent therapy in anthracycline- and taxane-pretreated metastatic breast cancer: results from nine randomized phase III trials. *Onco. Targets Ther.* **9**, 4061–4074 (2016).
7. Mauri, D., Polyzos, N. P., Salanti, G., Pavlidis, N. & Ioannidis, J. P. A. Multiple-treatments meta-analysis of chemotherapy and targeted therapies in advanced breast cancer. *J. Natl. Cancer Inst.* **100**, 1780–1791 (2008).
8. Damaraju, V. L. et al. Synergistic activity of troxacitabine (Troxatyl) and gemcitabine in pancreatic cancer. *BMC Cancer* **7**, 121 (2007).
9. Chou, T. C. Theoretical basis, experimental design, and computerized simulation of synergism and antagonism in drug combination studies. *Pharmacol. Rev.* **58**, 621–681 (2006).
10. Chang, T. T. & Chou, T. C. Rational approach to the clinical protocol design for drug combinations: A review. *Acta Paediatr. Taiwan* **41**, 294–302 (2000).
11. Flobak, Å. et al. A high-throughput drug combination screen of targeted small molecule inhibitors in cancer cell lines. *Sci. Data* https://doi.org/10.1038/s41597-019-0255-7 (2019).
12. Li, X. et al. Prediction of synergistic anti-cancer drug combinations based on drug target network and drug induced gene expression profiles. *Artif. Intell. Med.* **83**, 35–43 (2017).
13. Jeon, M., Kim, S., Park, S., Lee, H. & Kang, J. In silico drug combination discovery for personalized cancer therapy. *BMC Syst. Biol.* **12**, 16 (2018).
14. Celebi, R., Bear Don't Walk, O., Movva, R., Alpsoy, S. & Dumontier, M. In-silico prediction of synergistic anti-cancer drug combinations using multi-omics data. *Sci. Rep.* **9**, 8949 (2019).
15. Sidorov, P., Naulaerts, S., Ariey-Bonnet, J., Pasquier, E. & Ballester, P. J. Predicting synergism of cancer drug combinations using NCI-ALMANAC data. *Front. Chem.* **7**, 1–13 (2019).
16. Preuer, K. et al. DeepSynergy: Predicting anti-cancer drug synergy with deep learning. *Bioinformatics* **34**, 1538–1546 (2018).
17. Zhang, T., Zhang, L., Payne, P. R. O. & Li, F. Synergistic drug combination prediction by integrating multiomics data in deep learning models. *Methods Mol. Biol.* **2194**, 223–238 (2021).

18. Kuru, H. I., Tastan, O. & Cicek, A. E. MatchMaker: A deep learning framework for drug synergy prediction. *IEEE/ACM Trans. Comput. Biol. Bioinform.* **19**, 2334–2344 (2022).
19. Ma, J. & Motsinger-Reif, A. Prediction of synergistic drug combinations using PCA-initialized deep learning. *BioData Min.* **14**, 1–15 (2021).
20. Torkamannia, A., Omidi, Y. & Ferdousi, R. SYNDEEP: A deep learning approach for the prediction of cancer drugs synergy. *Sci. Rep.* **13**, 6184 (2023).
21. Preto, A. J., Matos-Filipe, P., Mourão, J. & Moreira, I. S. SYNPRED: Prediction of drug combination effects in cancer using different synergy metrics and ensemble learning. *Gigascience* **11**, giac087 (2022).
22. Srithanyarat, T. et al. Interpreting drug synergy in breast cancer with deep learning using target-protein inhibition profiles. *BioData Min.* **17**, 8 (2024).
23. Hu, J. et al. DTSyn: A dual-transformer-based neural network to predict synergistic drug combinations. *Brief. Bioinform.* https://doi.org/10.1093/bib/bbac302 (2022).
24. Liu, M., Srivastava, G., Ramanujam, J. & Brylinski, M. SynerGNet: A graph neural network model to predict anticancer drug synergy. *Biomolecules* **14**, 253 (2024).
25. Liu, X. et al. DrugFormer: Graph-enhanced language model to predict drug sensitivity. *Adv Sci* **11**, e2405861 (2024).
26. Besharatifard, M. & Vafaee, F. A review on graph neural networks for predicting synergistic drug combinations. *Artif. Intell. Rev.* **57**, 49 (2024).
27. Yang, J., Xu, Z., Wu, W. K. K., Chu, Q. & Zhang, Q. GraphSynergy: A network-inspired deep learning model for anticancer drug combination prediction. *J. Am. Med. Inform. Assoc.* **28**, 2336–2345 (2021).
28. Wang, J., Liu, X., Shen, S., Deng, L. & Liu, H. DeepDDS: Deep graph neural network with attention mechanism to predict synergistic drug combinations. *Brief Bioinform.* **23**, 1–11 (2022).
29. Zhang, H., Feng, J., Zeng, A., Payne, P. & Li, F. Predicting tumor cell response to synergistic drug combinations using a novel simplified deep learning model. *AMIA Annu. Symp. Proc.* **2020**, 1364–1372 (2020).
30. Zhang, H., Chen, Y. & Li, F. Predicting anticancer drug response with deep learning constrained by signaling pathways. *Front. Bioinform.* **1**, 639349 (2021).
31. Du, M., Liu, N. & Hu, X. Techniques for interpretable machine learning. *Commun. ACM* **63**, 68–77 (2019).
32. Wang, C., Kumar, G. A. & Rajapakse, J. C. Drug discovery and mechanism prediction with explainable graph neural networks. *Sci. Rep.* **15**, 179 (2025).
33. Sundararajan, M., Taly, A. & Yan, Q. Axiomatic attribution for deep networks. (2017).
34. Ying, R., Bourgeois, D., You, J., Zitnik, M. & Leskovec, J. GNNExplainer: generating explanations for graph neural networks. (2019).
35. Janizek, J. D., Celik, S. & Lee, S.-I. Explainable machine learning prediction of synergistic drug combinations for precision cancer medicine. *BioRxiv* https://doi.org/10.1101/331769 (2018).
36. Liu, Q. & Xie, L. TranSynergy: mechanism-driven interpretable deep neural network for the synergistic prediction and pathway deconvolution of drug combinations. *PLoS Comput. Biol.* **17**, e1008653 (2021).
37. Gómez Tejeda Zañudo, J. et al. Cell line-specific network models of ER+ breast cancer identify potential PI3Kα inhibitor resistance mechanisms and drug combinations. *Cancer Res.* **81**, 4603–4617 (2021).
38. Gómez Tejeda Zañudo, J., Scaltriti, M. & Albert, R. A network modeling approach to elucidate drug resistance mechanisms and predict combinatorial drug treatments in breast cancer. *Cancer Converg.* **1**, 5 (2017).
39. Niederdorfer, B. et al. Strategies to enhance logic modeling-based cell line-specific drug synergy prediction. *Front. Physiol.* **11**, 862 (2020).
40. Flobak, Å. et al. Discovery of drug synergies in gastric cancer cells predicted by logical modeling. *PLoS Comput. Biol.* **11**, 1–20 (2015).
41. Taoma, K., Ruengjitchatchawalya, M., Liangruksa, M. & Laomettachit, T. Boolean modeling of breast cancer signaling pathways uncovers mechanisms of drug synergy. *PLoS ONE* **19**, e0298788 (2024).
42. Tsirvouli, E. et al. A middle-out modeling strategy to extend a colon cancer logical model improves drug synergy predictions in epithelial-derived cancer cell lines. *Front. Mol. Biosci.* **7**, 502573 (2020).
43. Malyutina, A. et al. Drug combination sensitivity scoring facilitates the discovery of synergistic and efficacious drug combinations in cancer. *PLoS Comput. Biol.* **15**, e1006752 (2019).
44. Kanehisa, M. & Goto, S. KEGG: Kyoto encyclopedia of genes and genomes. *Nucleic Acids Res.* **28**, 27–30 (2000).
45. Kanehisa, M., Furumichi, M., Sato, Y., Matsuura, Y. & Ishiguro-Watanabe, M. KEGG: Biological systems database as a model of the real world. *Nucleic Acids Res.* **53**, D672–D677 (2025).
46. Apley, D. W. & Zhu, J. Visualizing the effects of predictor variables in black box supervised learning models. *J. R. Stat. Soc. Series B Stat. Methodol.* **82**, 1059–1086 (2020).
47. Yang, W. et al. Estrogen receptor alpha drives mTORC1 inhibitor-induced feedback activation of PI3K/AKT in ER+ breast cancer. *Oncotarget* **9**, 8810–8822 (2018).
48. Abdelnaby, R. M. et al. Dual PI3K/AKT inhibitors bearing Coumarin-Thiazolidine pharmacophores as potential apoptosis inducers in MCF-7 cells. *Pharmaceuticals* **15**, 428 (2022).
49. Adomas, A. B. et al. Breast tumor specific mutation in GATA3 affects physiological mechanisms regulating transcription factor turnover. *BMC Cancer* **14**, 278 (2014).
50. Ribas, R. et al. AKT antagonist AZD5363 influences estrogen receptor function in endocrine-resistant breast cancer and synergizes with fulvestrant (ICI182780) in vivo. *Mol. Cancer Ther.* **14**, 2035–2048 (2015).
51. Cowen, L., Ideker, T., Raphael, B. J. & Sharan, R. Network propagation: A universal amplifier of genetic associations. *Nat. Rev. Genet.* **18**, 551–562 (2017).
52. Carracedo, A. et al. Inhibition of mTORC1 leads to MAPK pathway activation through a PI3K-dependent feedback loop in human cancer. *J. Clin. Invest.* **118**, 3065–3074 (2008).
53. You, K. S., Yi, Y. W., Kwak, S. J. & Seong, Y. S. Inhibition of RPTOR overcomes resistance to EGFR inhibition in triple-negative breast cancer cells. *Int. J. Oncol.* **52**, 828–840 (2018).
54. Nagathihalli, N. S. et al. Inverse correlation of STAT3 and MEK signaling mediates resistance to RAS pathway inhibition in pancreatic cancer. *Cancer Res.* **78**, 6235–6246 (2018).
55. Zagozewski, J. et al. Combined MEK and JAK/STAT3 pathway inhibition effectively decreases SHH medulloblastoma tumor progression. *Commun. Biol.* **5**, 697 (2022).
56. Zheng, Z.-Y. et al. Blocking STAT3 signaling augments MEK/ERK inhibitor efficacy in esophageal squamous cell carcinoma. *Cell Death Dis.* **13**, 496 (2022).
57. Zou, Y. et al. Forkhead box transcription factor FOXO3a suppresses estrogen-dependent breast cancer cell proliferation and tumorigenesis. *Breast Cancer Res.* **10**, R21 (2008).
58. Stan, S. D., Hahm, E.-R., Warin, R. & Singh, S. V. Withaferin A causes FOXO3a- and Bim-dependent apoptosis and inhibits growth of human breast cancer cells in vivo. *Cancer Res.* **68**, 7661–7669 (2008).
59. Shin, S. et al. Glycogen synthase kinase-3β positively regulates protein synthesis and cell proliferation through the regulation of translation initiation factor 4E-binding protein 1. *Oncogene* **33**, 1690–1699 (2014).
60. de Graffenried, L. A. et al. NF-κB inhibition markedly enhances sensitivity of resistant breast cancer tumor cells to tamoxifen. *Ann. Oncol.* **15**, 885–890 (2004).

61. Frasor, J., El-Shennawy, L., Stender, J. D. & Kastrati, I. NFκB affects estrogen receptor expression and activity in breast cancer through multiple mechanisms. *Mol. Cell Endocrinol.* **418**(Pt 3), 235–239 (2015).
62. Li, X., Cao, Y., Li, M. & Jin, F. Upregulation of Hes1 promotes cell proliferation and invasion in breast cancer as a prognosis marker and therapy target via the AKT pathway and EMT process. *J. Cancer* **9**, 757–766 (2018).
63. House, R. R. J. et al. NF1 deficiency drives metabolic reprogramming in ER+ breast cancer. *Mol. Metab.* **80**, 101876 (2024).
64. Zhang, M. et al. NEDD4L in human tumors: Regulatory mechanisms and dual effects on anti-tumor and pro-tumor. *Front. Pharmacol.* **14**, 1291773 (2023).
65. Harrington, L. S. et al. The TSC1-2 tumor suppressor controls insulin-PI3K signaling via regulation of IRS proteins. *J Cell Biol* **166**, 213–223 (2004).
66. Park, R. K., Erdreich-Epstein, A., Liu, M., Izadi, K. D. & Durden, D. L. High affinity IgG receptor activation of Src family kinases is required for modulation of the Shc-Grb2-Sos complex and the downstream activation of the nicotinamide adenine dinucleotide phosphate (reduced) oxidase. *J. Immunol.* **163**, 6023–6034 (1999).
67. Fang, D. et al. Phosphorylation of beta-catenin by AKT promotes beta-catenin transcriptional activity. *J. Biol. Chem.* **282**, 11221–11229 (2007).
68. Ryu, W.-J. et al. Destabilization of β-catenin and RAS by targeting the Wnt/β-catenin pathway as a potential treatment for triple-negative breast cancer. *Exp. Mol. Med.* **52**, 832–842 (2020).
69. Wang, C.-C., Cirit, M. & Haugh, J. M. PI3K-dependent cross-talk interactions converge with RAS as quantifiable inputs integrated by ERK. *Mol. Syst. Biol.* **5**, 246 (2009).
70. Hayashi, H. et al. Centaurin-alpha1 is a phosphatidylinositol 3-kinase-dependent activator of ERK1/2 mitogen-activated protein kinases. *J. Biol. Chem.* **281**, 1332–1337 (2006).
71. Jang, K., Kim, M., Seo, H.-S. & Shin, I. PTEN sensitizes MDA-MB-468 cells to inhibition of MEK/ERK signaling for the blockade of cell proliferation. *Oncol. Rep.* **24**, 787–793 (2010).
72. Hoeflich, K. P. et al. In vivo antitumor activity of MEK and phosphatidylinositol 3-kinase inhibitors in basal-like breast cancer models. *Clin. Cancer Res.* **15**, 4649–4664 (2009).
73. Shah, H., Mistry, M., Patel, N. & Vora, H. Clinical significance of Notch receptors in triple negative breast cancer. *Breast Dis.* **42**, 85–100 (2023).
74. Yan, F., Wu, Z., Li, Z. & Liu, L. Celastrol inhibits migration and invasion of triple-negative breast cancer cells by suppressing Interleukin-6 via downregulating Nuclear Factor-κB (NF-κB). *Med. Sci. Monit.* **26**, e922814 (2020).
75. Liu, H. et al. S100A7 enhances invasion of human breast cancer MDA-MB-468 cells through activation of nuclear factor-κB signaling. *World J. Surg. Oncol.* **11**, 93 (2013).
76. Shibata, A. et al. Inhibition of NF-kappaB activity decreases the VEGF mRNA expression in MDA-MB-231 breast cancer cells. *Breast Cancer Res. Treat.* **73**, 237–243 (2002).
77. Murshed, F., Farhana, L., Dawson, M. I. & Fontana, J. A. NF-κB p65 recruited SHP regulates PDCD5-mediated apoptosis in cancer cells. *Apoptosis* **19**, 506–517 (2014).
78. Zhu, H. et al. Correlation of Notch1, pAKT and nuclear NF-κB expression in triple negative breast cancer. *Am. J. Cancer Res.* **3**, 230–239 (2013).
79. Ichimura, T. et al. 14-3-3 proteins modulate the expression of epithelial Na+ channels by phosphorylation-dependent interaction with Nedd4-2 ubiquitin ligase. *J. Biol. Chem.* **280**, 13187–13194 (2005).
80. Le, X. et al. Systematic functional characterization of resistance to PI3K inhibition in breast cancer. *Cancer Discov.* **6**, 1134–1147 (2016).
81. Xing, Y. et al. Phase II trial of AKT inhibitor MK-2206 in patients with advanced breast cancer who have tumors with PIK3CA or AKT mutations, and/or PTEN loss/PTEN mutation. *Breast Cancer Res.* **21**, 78 (2019).
82. Condorelli, R. et al. Polyclonal RB1 mutations and acquired resistance to CDK 4/6 inhibitors in patients with metastatic breast cancer. *Ann. Oncol.* **29**, 640–645 (2018).

Acknowledgements

K.T. acknowledges the Petchra Pra Jom Klao Ph.D. Research Scholarship (KMUTT – NSTDA) from King Mongkut's University of Technology Thonburi (No: 103/2563). This research project is supported by King Mongkut's University of Technology Thonburi (KMUTT), Thailand Science Research and Innovation (TSRI), and National Science, Research and Innovation Fund (NSRF) Fiscal year 2024 Grant number FRB670016/0164.

Author contributions

K.T., M.R., M.L., and T.L. conceived the conception of this study. K.T. and T.L. designed the methodology and performed analysis. All authors interpreted the results. K.T. wrote the first draft. All authors revised the manuscript. All authors read and approved the final manuscript.

Declarations

Competing interests

The authors declare no competing interests.

Additional information

Supplementary Information The online version contains supplementary material available at https://doi.org/10.1038/s41598-025-02444-7.

Correspondence and requests for materials should be addressed to T.L.

Reprints and permissions information is available at www.nature.com/reprints.

Publisher's note Springer Nature remains neutral with regard to jurisdictional claims in published maps and institutional affiliations.